Cell Reports

Report

Restoration of fitness lost due to dysregulation of the pyruvate dehydrogenase complex is triggered by ribosomal binding site modifications

Graphical abstract

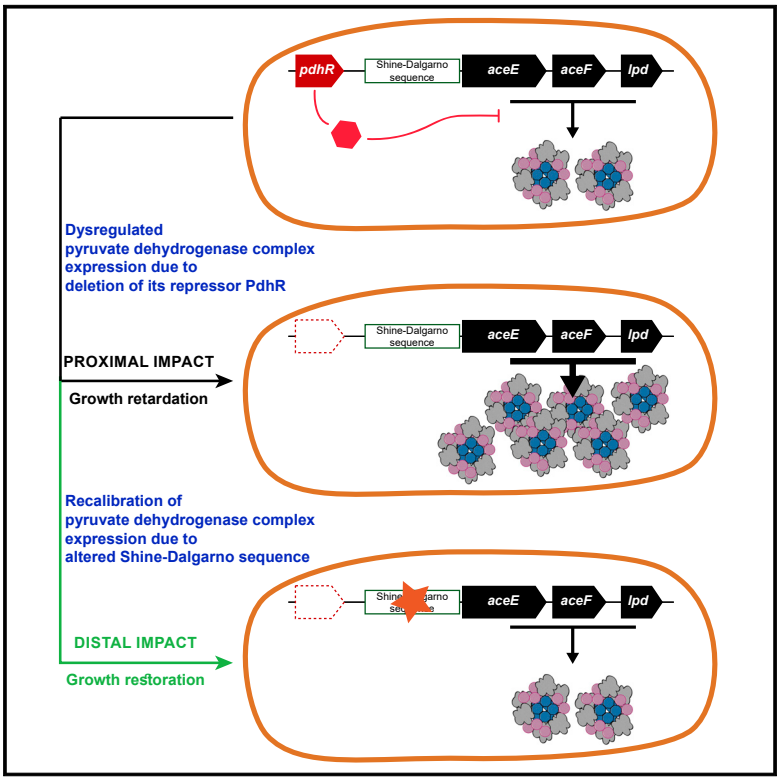

Highlights

- Pyruvate dehydrogenase regulator deletion compromises the growth-supporting proteome
- Shine-Dalgarno sequence mutations tailor expression levels of pyruvate dehydrogenase
- Bacteria find an alternate regulatory mechanism if the primary mode of regulation fails

Authors

Amitesh Anand, Connor A. Olson, Anand V. Sastry, ..., Laurence Yang, Adam M. Feist, Bernhard O. Palsson

Correspondence

palsson@ucsd.edu

In brief

Anand et al. show that the proximal effect of a proteome imbalance and consequent growth retardation from dysregulated expression of the pyruvate dehydrogenase complex is mitigated by an adaptive alteration in the efficiency of the ribosome recruitment.

Anand et al., 2021, Cell Reports *35*, 108961
April 6, 2021
https://doi.org/10.1016/j.celrep.2021.108961

CellPress

Cell Reports

CellPress
OPEN ACCESS

Report

Restoration of fitness lost due to dysregulation of the pyruvate dehydrogenase complex is triggered by ribosomal binding site modifications

Amitesh Anand,[1] Connor A. Olson,[1] Anand V. Sastry,[1] Arjun Patel,[1] Richard Szubin,[1] Laurence Yang,[1,2] Adam M. Feist,[1,3] and Bernhard O. Palsson[1,3,4,*]

[1]Department of Bioengineering, University of California, San Diego, La Jolla, CA 92093, USA
[2]Department of Chemical Engineering, Queen's University, Kingston, ON, Canada
[3]Novo Nordisk Foundation Center for Biosustainability, Technical University of Denmark, Kemitorvet, Building 220, 2800 Kongens, Lyngby, Denmark
[4]Lead contact
*Correspondence: palsson@ucsd.edu
https://doi.org/10.1016/j.celrep.2021.108961

SUMMARY

Pyruvate dehydrogenase complex (PDC) functions as the main determinant of the respiro-fermentative balance because it converts pyruvate to acetyl-coenzyme A (CoA), which then enters the TCA (tricarboxylic acid cycle). PDC is repressed by the pyruvate dehydrogenase complex regulator (PdhR) in *Escherichia coli*. The deletion of the *pdhR* gene compromises fitness in aerobic environments. We evolve the *E. coli pdhR* deletion strain to examine its achievable growth rate and the underlying adaptive strategies. We find that (1) optimal proteome allocation to PDC is critical in achieving optimal growth rate; (2) expression of PDC in evolved strains is reduced through mutations in the Shine-Dalgarno sequence; (3) rewiring of the TCA flux and increased reactive oxygen species (ROS) defense occur in the evolved strains; and (4) the evolved strains adapt to an efficient biomass yield. Together, these results show how adaptation can find alternative regulatory mechanisms for a key cellular process if the primary regulatory mode fails.

INTRODUCTION

The metabolic link between glycolysis and the tricarboxylic acid cycle (TCA) is established by the oxidative decarboxylation of pyruvate to acetyl-coenzyme A (CoA) catalyzed by the multienzyme, pyruvate dehydrogenase complex (PDC). The PDC in all known living organisms is composed of multiple copies of three catalytic enzymes: pyruvate dehydrogenase, dihydrolipoamide acetyltransferase, and dihydrolipoamide dehydrogenase (Patel et al., 2014). This multi-enzyme assembly enables a highly coordinated catalytic activity that prevents intermediate products from diffusing, ensuring the completion of the reaction (Pelley, 2011). Because of its crucial physiological significance, the expression and function of PDC are tightly regulated. In *Escherichia coli*, PDC is transcriptionally regulated by the transcription factor PdhR, which represses its expression. Interestingly, PdhR has now been shown to have a larger effect on cellular physiology, ranging from energy maintenance to redox homeostasis, and the loss of this regulator limits the aerobic growth capabilities of *E. coli* (Göhler et al., 2011; Maeda et al., 2017; Ogasawara et al., 2007).

Here, we performed a systemic study to examine the growth bottleneck in the *pdhR* deletion strain and delineated the adaptive response to the loss of PdhR regulation. We observed the resource partitioning from the increased expression of the multienzyme PDC as the factor limiting the growth-supporting proteome. The adaptive laboratory evolution (ALE) of the Δ*pdhR* strain resulted from mutations in the Shine-Dalgarno sequence of pyruvate dehydrogenase, which re-calibrated the PDC expression levels and restored the optimal growth. We also observed a rewiring in the TCA flux and oxidative stress response pathways, which allowed an efficient biomass yield in the evolved strains. Thus, the distal effect of the *pdhR* deletion is distinct from the proximal manifestation, reflecting the tenacity of microbial systems.

RESULTS AND DISCUSSION

Proximal effect of pyruvate node dysregulation

The PDC of *E. coli* has a mass of 4.5 MDa and has 60 subunits (AceE:AceF:Lpd::24:24:12) assembled in an octahedral symmetry (Patel et al., 2014). We observed an approximately 4-fold upregulation of this large enzyme complex in the *pdhR* deletion strain (Figure 1A). Unregulated expression of such costly proteome components can limit resources available for other cellular functions and impair the robustness of the metabolic network (Lloyd et al., 2020). We examined this potential trade-off using a genome-scale model of metabolism and macromolecular expression, iJL1678b-ME (Lloyd et al., 2018). We simulated the maximum growth rate of *E. coli*

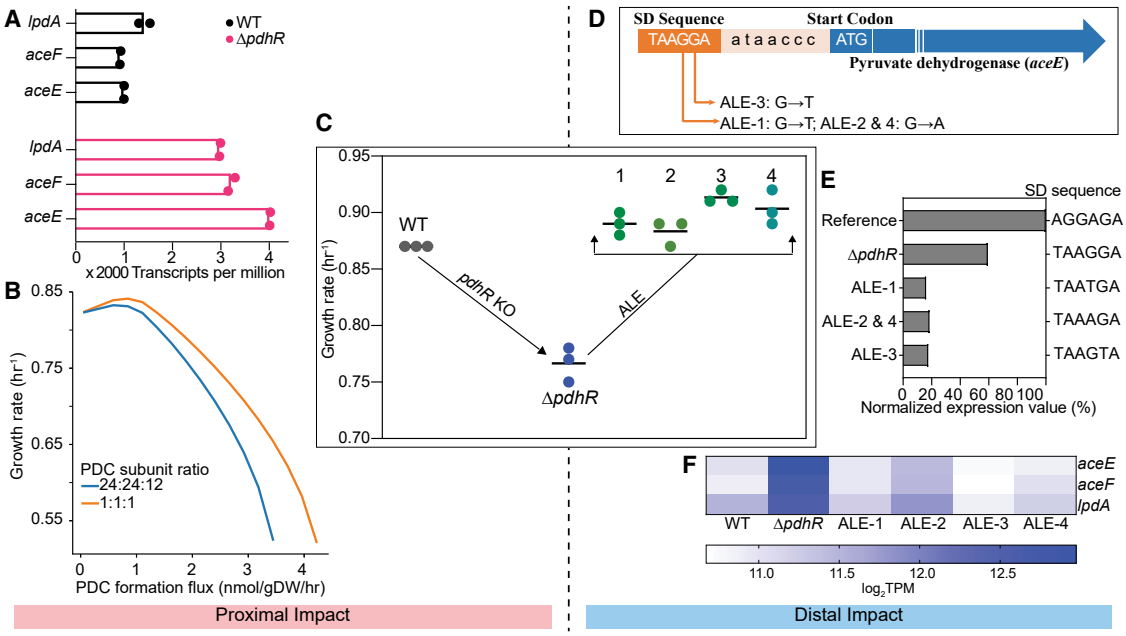

Figure 1. Effect of pyruvate node dysregulation and laboratory evolution to regain optimal function

(A) Transcriptional status of the PDC upon deletion of PdhR.

(B) Growth rate trade-off corresponding to the expression of PDC estimated by the metabolism and macromolecular expression (ME) model.

(C) Growth rates of the four independently evolved lineages of the Δ*pdhR* strain after approximately 300 generations. Plot displays values of the three biological replicates along with their means.

(D) The convergent mutation in the independently evolved lineages of the Δ*pdhR* strain.

(E) Computational model-based prediction of expression potential of the alternate SD sequences created during ALE. The "reference" SD sequence is the EMOPEC-derived sequence for the maximum expression of the gene.

(F) Heatmap showing expression levels (in terms of transcripts per million [TPM]) of PDC in the reference and evolved strains. The color intensity of the scale indicates the binary logarithm of TPM counts.

over a range of specified PDC formation rates, ranging from approximately 0.1 to 20 times the optimal formation rate corresponding to maximum growth on glucose-minimal medium. We found a negative correlation between the systems-level cost of PDC formation and the growth rate (Figure 1B). We also examined whether the large size of PDC exacerbates its effect on the growth rate at high expression levels. Using the genome-scale model, we modified the PDC to consist only of three monomers: a single copy each of AceE, AceF, and Lpd. We then performed the same simulation and used the same effective turnover rate (number of reactions per time per complex) as that of the normal PDC. Simulations showed that the smaller PDC would increase the *E. coli* maximum growth rate. Therefore, the cost of PDC synthesis is greater because of its large size, and that expression cost directly affects the growth rate.

Optimal fitness restoration revealed by adaptive laboratory evolution

The loss of PdhR activity in the Δ*pdhR* strain resulted in more than a 20% growth retardation. Bacterial systems possess a certain degree of plasticity, which allows them to explore ways to achieve optimal fitness (Bershtein et al., 2015; Rodrigues and Shakhnovich, 2019). We examined achievable growth improvement in the Δ*pdhR* strain by performing ALE (Gresham and Dunham, 2014; Long and Antoniewicz, 2018; Remigi et al., 2019). In about 300 generations of ALE, we observed a significant growth restoration. Invariably, every independent replicate reached an optimal growth rate (≥0.9 h^{-1}) (Figure 1C).

The fitness improvement motivated us to find beneficial compensatory mutations in the evolved strains. We performed whole-genome sequencing of all the evolved strains and carefully compared the genome content against the starting strain (Deatherage and Barrick, 2014). Every evolved replicate acquired two or three mutations and, interestingly, the 5′ untranslated region (5′ UTR) of pyruvate dehydrogenase (*aceE*) was mutated in all four evolved replicates, indicating a causal nature for this sequence change (Figure 1D; Table S1). We introduced the mutation observed in the evolved strain into the Δ*pdhR* strain and performed comparative growth profiling (Figure S1A). This confirmed the causal relationship between mutation and fitness improvement.

In *E. coli*, the ribosome binding site is typically located eight to 10 bases upstream of the translation initiation codon and contains a polypurine domain known as the Shine-Dalgarno (SD) sequence (Chen et al., 1994; Ringquist et al., 1992). The *aceE* gene contains a short SD sequence of UAAGGA located seven bases upstream of the start codon AUG. Every Δ*pdhR* evolved strain invariably substituted guanine in the SD region for either

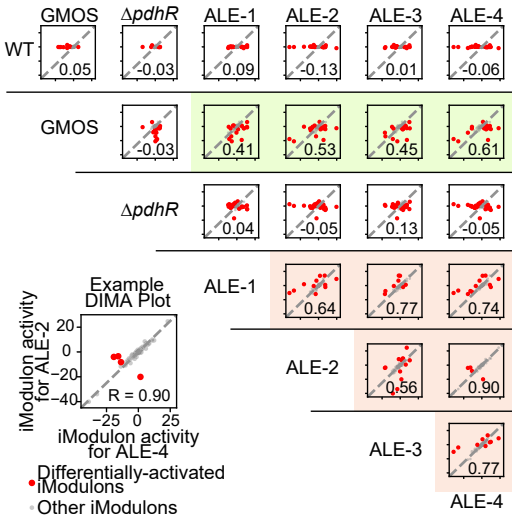

Figure 2. Differential iModulon activity plots (DIMA) showing transcriptional similarities among various strains of this study

All DIMA plots (Kavvas et al., 2020; Sastry et al., 2019) have the same scale on the x and y axes, which can be seen in the example plot. Δ*pdhR*-evolved replicates showed a high positive correlation among themselves and with the media-adapted GMOS strain, but the transcriptome was poorly correlated with Δ*pdhR* or the unevolved WT strain.

adenine or thymine, decreasing the base-pairing potential of the region. Interestingly, the gene expression has a significant correlation with the SD sequence (Lim et al., 2016; Ma et al., 2002), and these mutations could be a potential mechanism with which the expression of the PDC is calibrated in the absence of its cognate regulator PdhR.

We estimated the thermodynamic properties of the translation initiation region of pyruvate dehydrogenase using a UTR designer (Seo et al., 2013). Every evolved replicate was predicted to have a relatively greater free-energy change upon ribosome binding and a consequent decrease in the expression of the gene (Table S2). This analysis was further supported by an SD-sequence engineering-specific predictive computational model EMOPEC (Empirical Model and Oligos for Protein Expression Changes) (Figure 1E) (Bonde et al., 2016). Therefore, to directly assess the evolved strain, we examined the transcript level of genes of the PDC and observed a significant decrease in the expression levels in the evolved strains as compared with those of the parent strain (Figure 1F). We further performed a pyruvate dehydrogenase activity assay, which showed a similar decrease of PDC at the protein levels as well (Figure S1B).

Further, the transcriptome of the evolved strain significantly diverged from the starting strain, and a strong positive correlation was observed among the independently evolved replicates themselves (Figure 2). Interestingly, the evolved strains showed a significant positive correlation with the glucose minimal-media-optimized strain (GMOS) of wild-type (WT) *E. coli* (Anand et al., 2020; LaCroix et al., 2015), suggesting an attempt to achieve optimal transcriptional status for faster growth.

Optimization of respiratory electron dissipation

Because PdhR is reported to regulate the components of the respiratory electron transport chain, we examined the transcriptional status of the respiratory quinone redox node in the *E. coli* genome-scale metabolic network reconstruction, iJO1366, using Escher (Figures 3A and S2A) (King et al., 2015; Orth et al., 2011). Both reduction and oxidation arms of the node showed an operational variation between the starting strain and the evolved strains of Δ*pdhR*. PdhR derepression in Δ*pdhR* resulted in increased transcription of type II NADH dehydrogenase; however, the levels decreased to WT levels in the evolved strains. Among cytochrome oxidases, cytochrome bo_3 oxidase showed variable transcriptional behavior in the evolved replicates. The expression of alternate cytochrome oxidases (cytochrome bd-I and bd-II) increased in the evolved strains. Notably, the reactive oxygen species (ROS)-protective cytochrome bd-II oxidase expression increased specifically in the evolved strains, except ALE-1 (Figure S2B) (Giuffrè et al., 2014). The *oxyR* mutation in ALE-1 likely improved the ROS tolerance of the strain, which may be responsible for the non-reliance on cytochrome bd-II oxidase in this strain (Figure S2C) (Anand et al., 2020).

Interestingly, ALE after the deletion of the regulator of canonical pyruvate metabolizing enzymes resulted in increased expression of pyruvate oxidase (PoxB), the enzyme catalyzing the oxidative decarboxylation-based route of pyruvate metabolism. The periplasmic diversion of the pyruvate metabolism contributes to cellular redox homeostasis (Moreau, 2004) and improves the aerobic fitness of the strain (Li et al., 2007). This RpoS-regulated enzyme can form a ubiquinone-mediated redox loop with cytochrome oxidases and can potentially synergize respiratory electron shuttling (Carter and Gennis, 1985; Koland et al., 1984).

Redox homeostasis and metabolic rewiring

Previously, RpoS has been observed to drive periplasmic ROS mitigation to support the electron-transport system (ETS) operation (Anand et al., 2019a). We, therefore, used independent component analysis to estimate the activity of the RpoS iModulon (an iModulon is a set of independently modulated genes that often share the same transcriptional regulator) (Sastry et al., 2019). Every evolved replicate showed increased activity of the RpoS iModulon (Figure 3B). IraP is the anti-adaptor protein of RpoS and prevents targeting of RpoS to ClpXP protease (Bougdour et al., 2006; Girard et al., 2017). Interestingly, the expression of *iraP* increased specifically in the Δ*pdhR*-evolved strains and showed an expression pattern similar to RpoS iModulon activity, suggesting its involvement in the regulation of RpoS activity in these strains (Figure 3B). Additionally, we observed the repression of *nadB*, the largest contributor to cellular peroxide production (Korshunov and Imlay, 2010), specifically in the Δ*pdhR*-evolved strains (Figure S2B). These activity changes were supported by the efficient redox mitigation ability of the evolved strains, despite an increase in the growth rate (Figure 3C).

There is a fear-greed trade-off that fulfills the growth objective of a cell by shifting metabolic resources toward growth-related functions and away from stress-defense functions (Utrilla et al., 2016). We observed an unexpected trend in the translation

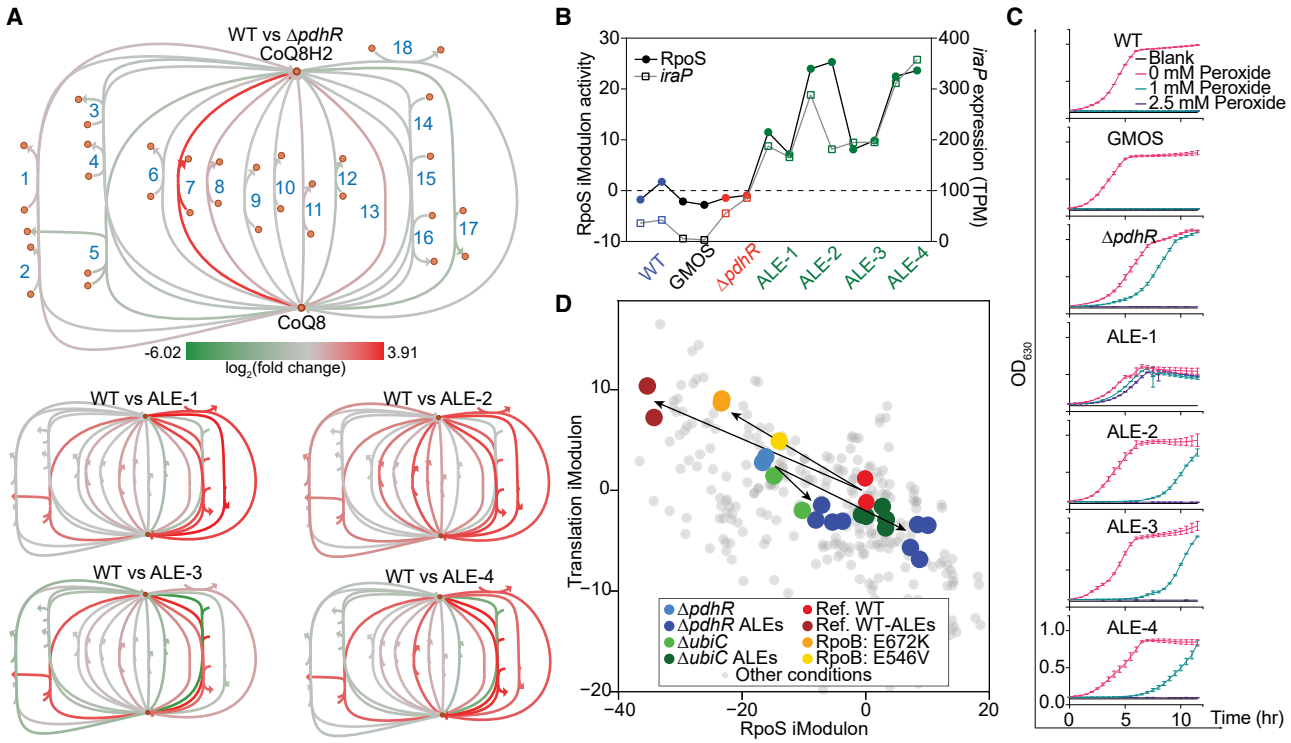

Figure 3. Metabolic recalibration after adaptive laboratory evolution

(A) Visualization of transcriptional status of the respiratory quinone redox node using Escher. From left to right, the reactions are as follows: (1) glucose dehydrogenase, (2) DsbA protein reoxidation reaction, (3) NADH dehydrogenase type I, (4) formate dehydrogenase, (5) hydrogenase, (6) NADPH quinone reductase, (7) NADH dehydrogenase type II, (8) D-lactate dehydrogenase, (9) pyruvate oxidase, (10) glycerol-3-phosphate dehydrogenase, (11) glycolate oxidase, (12) L-lactate dehydrogenase, (13) quinol monooxygenase, (14) cytochrome bo3 oxidase, (15) cytochrome bd oxidase, (16) nitrate reductase (H-pumping), (17) nitrate reductase, and (18) nitrite reductase.

(B) Independent component analysis (ICA)-derived activities of RpoS iModulon and expression pattern of the *iraP* gene.

(C) Peroxide sensitivity estimates of the strains in this study assessed by exposing the strains to different concentrations of hydrogen peroxide. Plot displays means and standard deviation of the three independent replicates.

(D) Trade-offs between translation and RpoS iModulons activities showing alternate adaptive optimization of fear versus greed in the evolved Δ*pdhR* strains to achieve efficient growth capabilities. The eight deep-blue dots are the four ALE endpoints in duplicate and the light-blue dots are pre-evolved Δ*pdhR* strains. As a comparison, we show the WT, the evolved WT, the *rpoB* mutants, and the laboratory-evolved Δ*ubiC* strains from two previously published studies (Anand et al., 2019a; Sastry et al., 2019).

versus RpoS iModulons activity-correlation plot (Sastry et al., 2019); the Δ*pdhR*-evolved strains favored RpoS activity over translation activity while improving their growth rate (Figure 3D). This trade-off pattern was substantiated by observing a similar behavior in naphthoquinone-based strains (Δ*ubiC* ALEs), in which RpoS activity is known to facilitate growth improvement (Anand et al., 2019a). The Δ*pdhR*-evolved strains appear to be finding an alternative trade-off to maintain RpoS-orchestrated ROS defense potential and achieve a higher growth rate.

Deletion of PdhR has been shown to improve glucose use in oxygen-limited conditions (Maeda et al., 2017); therefore, we examined the status of the central carbon metabolism in Δ*pdhR* strains evolved in an oxygen-rich environment. We incorporated the transcriptomics data and experimentally measured metabolite exchange rates into a genome-scale model of metabolism and protein expression to simulate the flux map (Figures 4 and S3) (Chen et al., 2017). We observed an overall upshift in the central metabolism of the evolved strains. Notably, the growth-rate improvement in the Δ*pdhR*-evolved strains, unlike that in the WT strain evolution, was not accompanied by acetate overflow metabolism (Table S3). In addition, the glycolytic flux in the Δ*pdhR* evolved strains continued to rely on the Embden-Meyerhof-Parnas (EMP) pathway, unlike that in the WT evolution, in which the adaptation to glucose minimal media activated the Entner-Doudoroff (ED) pathway. The ED pathway, although yielding less ATP, results in a NADPH formation, which could be advantageous to oxidative stress mitigation in fast-growing strains (Chavarría et al., 2013; Klingner et al., 2015; Mendoza-Chamizo et al., 2018). The RpoS-dependent redox stress tolerance may be enabling a continued dominance of the high-ATP-yielding glycolytic pathway in these strains.

Conclusions

Taken together, we used a combination of complementary experimental and computational systems-level approaches to

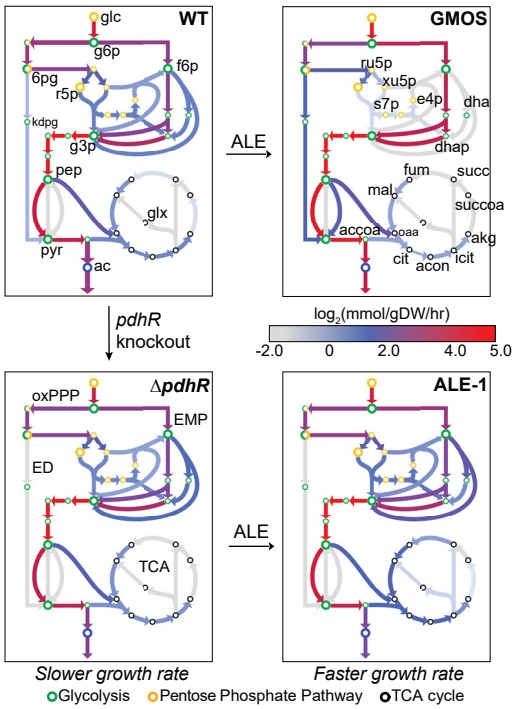

Figure 4. Optimization of glycolytic and TCA efficiency

Computed metabolic flux maps depicting the central metabolism in the WT, GMOS, the pre-evolved, and the evolved Δ*pdhR* strains. Key metabolites indicated in the figure are as follows: glc, glucose; g6p, D-glucose-6-phosphate; g3p, glyceraldehyde-3-phosphate; f6p, D-fructose-6-phosphate; 6pgc, 6-phospho-D-gluconate; r5p, α-D-ribose 5-phosphate; pep, phosphoenolpyruvate; pyr, pyruvate; ac, acetate. Calculated fluxes of each strain are colored on a log scale.

discover that mutations in the SD sequence relieve the growth restriction resulting from the dysregulation of PDC expression. We identified the metabolic rewiring and stress rebalancing needed to achieve the carbon-conservative bioenergetics leading to the restoration of optimal growth. This study, thus, reveals how distal causation, manifested during laboratory evolution, creates alternative regulatory mechanisms for a key cellular process if the primary mode of regulation fails.

STAR★METHODS

Detailed methods are provided in the online version of this paper and include the following:

SUPPLEMENTAL INFORMATION

Supplemental information can be found online at https://doi.org/10.1016/j.celrep.2021.108961.

ACKNOWLEDGMENTS

This work was funded by the Novo Nordisk Foundation grant no. NNF10CC1016517 and National Institutes of Health grants R01GM057089 and U01AI124316. We would like to thank Marc Abrams (Systems Biology Research Group, University of California, San Diego) for his assistance with manuscript editing.

AUTHOR CONTRIBUTIONS

A.A. and B.O.P. designed the study. A.A., C.A.O., and R.S. performed the experiments. A.A., A.V.S, A.P., L.Y., and A.M.F. analyzed the data. A.A. and B.O.P. wrote the manuscript, with contributions from all the other co-authors.

DECLARATION OF INTERESTS

The authors declare no competing interests.

Received: September 8, 2020
Revised: February 22, 2021
Accepted: March 16, 2021
Published: April 6, 2021

REFERENCES

Anand, A., Chen, K., Yang, L., Sastry, A.V., Olson, C.A., Poudel, S., Seif, Y., Hefner, Y., Phaneuf, P.V., Xu, S., et al. (2019a). Adaptive evolution reveals a tradeoff between growth rate and oxidative stress during naphthoquinone-based aerobic respiration. Proc. Natl. Acad. Sci. USA *116*, 25287–25292.

Anand, A., Olson, C.A., Yang, L., Sastry, A.V., Catoiu, E., Choudhary, K.S., Phaneuf, P.V., Sandberg, T.E., Xu, S., Hefner, Y., et al. (2019b). Pseudogene repair driven by selection pressure applied in experimental evolution. Nat. Microbiol. *4*, 386–389.

Anand, A., Chen, K., Catoiu, E., Sastry, A.V., Olson, C.A., Sandberg, T.E., Seif, Y., Xu, S., Szubin, R., Yang, L., et al. (2020). OxyR is a convergent target for mutations acquired during adaptation to oxidative stress-prone metabolic states. Mol. Biol. Evol. *37*, 660–667.

Baba, T., Ara, T., Hasegawa, M., Takai, Y., Okumura, Y., Baba, M., Datsenko, K.A., Tomita, M., Wanner, B.L., and Mori, H. (2006). Construction of *Escherichia coli* K-12 in-frame, single-gene knockout mutants: the Keio collection. Mol. Syst. Biol. *2*, 0008.

Bershtein, S., Choi, J.-M., Bhattacharyya, S., Budnik, B., and Shakhnovich, E. (2015). Systems-level response to point mutations in a core metabolic enzyme modulates genotype-phenotype relationship. Cell Rep. *11*, 645–656.

Bonde, M.T., Pedersen, M., Klausen, M.S., Jensen, S.I., Wulff, T., Harrison, S., Nielsen, A.T., Herrgård, M.J., and Sommer, M.O.A. (2016). Predictable tuning of protein expression in bacteria. Nat. Methods *13*, 233–236.

Bougdour, A., Wickner, S., and Gottesman, S. (2006). Modulating RssB activity: IraP, a novel regulator of σ^S stability in *Escherichia coli*. Genes Dev. *20*, 884–897.

Carter, K., and Gennis, R.B. (1985). Reconstitution of the ubiquinone-dependent pyruvate oxidase system of *Escherichia coli* with the cytochrome o terminal oxidase complex. J. Biol. Chem. *260*, 10986–10990.

Chavarría, M., Nikel, P.I., Pérez-Pantoja, D., and de Lorenzo, V. (2013). The Entner-Doudoroff pathway empowers *Pseudomonas putida* KT2440 with a high tolerance to oxidative stress. Environ. Microbiol. *15*, 1772–1785.

Chen, H., Bjerknes, M., Kumar, R., and Jay, E. (1994). Determination of the optimal aligned spacing between the Shine-Dalgarno sequence and the translation initiation codon of *Escherichia coli* mRNAs. Nucleic Acids Res. *22*, 4953–4957.

Chen, K., Gao, Y., Mih, N., O'Brien, E.J., Yang, L., and Palsson, B.O. (2017). Thermosensitivity of growth is determined by chaperone-mediated proteome reallocation. Proc. Natl. Acad. Sci. USA *114*, 11548–11553.

Deatherage, D.E., and Barrick, J.E. (2014). Identification of mutations in laboratory-evolved microbes from next-generation sequencing data using breseq. Methods Mol. Biol. *1151*, 165–188.

Girard, M.E., Gopalkrishnan, S., Grace, E.D., Halliday, J.A., Gourse, R.L., and Herman, C. (2017). DksA and ppGpp regulate the σ^S stress response by activating promoters for the small RNA DsrA and the anti-adapter protein IraP. J. Bacteriol. *200*, e00453-17.

Giuffrè, A., Borisov, V.B., Arese, M., Sarti, P., and Forte, E. (2014). Cytochrome bd oxidase and bacterial tolerance to oxidative and nitrosative stress. Biochim. Biophys. Acta *1837*, 1178–1187.

Glenn, T.C., Nilsen, R.A., Kieran, T.J., Sanders, J.G., Bayona-Vásquez, N.J., Finger, J.W., Pierson, T.W., Bentley, K.E., Hoffberg, S.L., Louha, S., et al. (2019). Adapterama I: universal stubs and primers for 384 unique dual-indexed or 147,456 combinatorially-indexed Illumina libraries (iTru & iNext). PeerJ *7*, e7755.

Göhler, A.-K., Kökpinar, Ö., Schmidt-Heck, W., Geffers, R., Guthke, R., Rinas, U., Schuster, S., Jahreis, K., and Kaleta, C. (2011). More than just a metabolic regulator—elucidation and validation of new targets of PdhR in *Escherichia coli*. BMC Syst. Biol. *5*, 197.

Gresham, D., and Dunham, M.J. (2014). The enduring utility of continuous culturing in experimental evolution. Genomics *104* (*6 Pt A*), 399–405.

Kavvas, E.S., Antoniewicz, M., Long, C., Ding, Y., Monk, J.M., Palsson, B.O., and Feist, A.M. (2020). Laboratory evolution of multiple *E. coli* strains reveals unifying principles of adaptation but diversity in driving genotypes. bioRxiv. https://doi.org/10.1101/2020.05.19.104992.

King, Z.A., Dräger, A., Ebrahim, A., Sonnenschein, N., Lewis, N.E., and Palsson, B.O. (2015). Escher: a web application for building, sharing, and embedding data-rich visualizations of biological pathways. PLoS Comput. Biol. *11*, e1004321.

Klingner, A., Bartsch, A., Dogs, M., Wagner-Döbler, I., Jahn, D., Simon, M., Brinkhoff, T., Becker, J., and Wittmann, C. (2015). Large-Scale 13C flux profiling reveals conservation of the Entner-Doudoroff pathway as a glycolytic strategy among marine bacteria that use glucose. Appl. Environ. Microbiol. *81*, 2408–2422.

Koland, J.G., Miller, M.J., and Gennis, R.B. (1984). Reconstitution of the membrane-bound, ubiquinone-dependent pyruvate oxidase respiratory chain of *Escherichia coli* with the cytochrome d terminal oxidase. Biochemistry *23*, 445–453.

Korshunov, S., and Imlay, J.A. (2010). Two sources of endogenous hydrogen peroxide in *Escherichia coli*. Mol. Microbiol. *75*, 1389–1401.

LaCroix, R.A., Sandberg, T.E., O'Brien, E.J., Utrilla, J., Ebrahim, A., Guzman, G.I., Szubin, R., Palsson, B.O., and Feist, A.M. (2015). Use of adaptive laboratory evolution to discover key mutations enabling rapid growth of *Escherichia coli* K-12 MG1655 on glucose minimal medium. Appl. Environ. Microbiol. *81*, 17–30.

Li, M., Yao, S., and Shimizu, K. (2007). Effect of *poxB* gene knockout on metabolism in *Escherichia coli* based on growth characteristics and enzyme activities. World J. Microbiol. Biotechnol. *23*, 573–580.

Lim, H.G., Noh, M.H., Jeong, J.H., Park, S., and Jung, G.Y. (2016). Optimum rebalancing of the 3-hydroxypropionic acid production pathway from glycerol in *Escherichia coli*. ACS Synth. Biol. *5*, 1247–1255.

Little, S. (2001). Amplification-refractory mutation system (ARMS) analysis of point mutations. Curr. Protoc. Hum. Genet. *Chapter 9*, Unit 9.8.

Lloyd, C.J., Ebrahim, A., Yang, L., King, Z.A., Catoiu, E., O'Brien, E.J., Liu, J.K., and Palsson, B.O. (2018). COBRAme: A computational framework for genome-scale models of metabolism and gene expression. PLoS Comput. Biol. *14*, e1006302.

Lloyd, C.J., Monk, J., Yang, L., Ebrahim, A., and Palsson, B.O. (2020). Computation of condition-dependent proteome allocation reveals variability in the macro and micro nutrient requirements for growth. bioRxiv. https://doi.org/10.1101/2020.03.23.003236.

Long, C.P., and Antoniewicz, M.R. (2018). How adaptive evolution reshapes metabolism to improve fitness: recent advances and future outlook. Curr. Opin. Chem. Eng. *22*, 209–215.

Ma, J., Campbell, A., and Karlin, S. (2002). Correlations between Shine-Dalgarno sequences and gene features such as predicted expression levels and operon structures. J. Bacteriol. *184*, 5733–5745.

Maeda, S., Shimizu, K., Kihira, C., Iwabu, Y., Kato, R., Sugimoto, M., Fukiya, S., Wada, M., and Yokota, A. (2017). Pyruvate dehydrogenase complex regulator (PdhR) gene deletion boosts glucose metabolism in *Escherichia coli* under oxygen-limited culture conditions. J. Biosci. Bioeng. *123*, 437–443.

Marotz, C., Amir, A., Humphrey, G., Gaffney, J., Gogul, G., and Knight, R. (2017). DNA extraction for streamlined metagenomics of diverse environmental samples. Biotechniques *62*, 290–293.

Mendoza-Chamizo, B., Løbner-Olesen, A., and Charbon, G. (2018). Coping with reactive oxygen species to ensure genome stability in *Escherichia coli*. Genes (Basel) *9*, 565.

Moreau, P.L. (2004). Diversion of the metabolic flux from pyruvate dehydrogenase to pyruvate oxidase decreases oxidative stress during glucose metabolism in nongrowing *Escherichia coli* cells incubated under aerobic, phosphate starvation conditions. J. Bacteriol. *186*, 7364–7368.

Ogasawara, H., Ishida, Y., Yamada, K., Yamamoto, K., and Ishihama, A. (2007). PdhR (pyruvate dehydrogenase complex regulator) controls the respiratory electron transport system in *Escherichia coli*. J. Bacteriol. *189*, 5534–5541.

Orth, J.D., Conrad, T.M., Na, J., Lerman, J.A., Nam, H., Feist, A.M., and Palsson, B.Ø. (2011). A comprehensive genome-scale reconstruction of *Escherichia coli* metabolism—2011. Mol. Syst. Biol. *7*, 535.

Patel, M.S., Nemeria, N.S., Furey, W., and Jordan, F. (2014). The pyruvate dehydrogenase complexes: structure-based function and regulation. J. Biol. Chem. *289*, 16615–16623.

Pelley, J.W. (2011). Elsevier's Integrated Review Biochemistry E-Book: With Student Consult Online Access (Elsevier Health Sciences).

Remigi, P., Masson-Boivin, C., and Rocha, E.P.C. (2019). Experimental evolution as a tool to investigate natural processes and molecular functions. Trends Microbiol. *27*, 623–634.

Ringquist, S., Shinedling, S., Barrick, D., Green, L., Binkley, J., Stormo, G.D., and Gold, L. (1992). Translation initiation in *Escherichia coli*: sequences within the ribosome-binding site. Mol. Microbiol. *6*, 1219–1229.

Rodrigues, J.V., and Shakhnovich, E.I. (2019). Adaptation to mutational inactivation of an essential gene converges to an accessible suboptimal fitness peak. Elife *8*, e50509.

Sastry, A.V., Gao, Y., Szubin, R., Hefner, Y., Xu, S., Kim, D., Choudhary, K.S., Yang, L., King, Z.A., and Palsson, B.O. (2019). The *Escherichia coli* transcriptome mostly consists of independently regulated modules. Nat. Commun. *10*, 5536.

Scott, M., Gunderson, C.W., Mateescu, E.M., Zhang, Z., and Hwa, T. (2010). Interdependence of cell growth and gene expression: origins and consequences. Science *330*, 1099–1102.

Scott, M., Klumpp, S., Mateescu, E.M., and Hwa, T. (2014). Emergence of robust growth laws from optimal regulation of ribosome synthesis. Mol. Syst. Biol. *10*, 747.

Seo, S.W., Yang, J.-S., Kim, I., Yang, J., Min, B.E., Kim, S., and Jung, G.Y. (2013). Predictive design of mRNA translation initiation region to control prokaryotic translation efficiency. Metab. Eng. *15*, 67–74.

Thomason, L.C., Costantino, N., and Court, D.L. (2007). *E. coli* genome manipulation by P1 transduction. Curr. Protoc. Mol. Biol. *Chapter 1*, Unit 1.17.

Utrilla, J., O'Brien, E.J., Chen, K., McCloskey, D., Cheung, J., Wang, H., Armenta-Medina, D., Feist, A.M., and Palsson, B.O. (2016). Global rebalancing of cellular resources by pleiotropic point mutations illustrates a multi-scale mechanism of adaptive evolution. Cell Syst. *2*, 260–271.

Zhao, D., Yuan, S., Xiong, B., Sun, H., Ye, L., Li, J., Zhang, X., and Bi, C. (2016). Development of a fast and easy method for *Escherichia coli* genome editing with CRISPR/Cas9. Microb. Cell Fact. *15*, 205.

STAR★METHODS

KEY RESOURCES TABLE

REAGENT or RESOURCE	SOURCE	IDENTIFIER
Bacterial and virus strains		
Escherichia coli K-12 MG1655	ATCC	ATCC 700926
Escherichia coli K12 MG1655 Δ*pdhR*	SBRG, University of California San Diego	PMID: 31767748
Escherichia coli K12 MG1655 Δ*pdhR* ALE-1	This paper	A13F51I1R1
Escherichia coli K12 MG1655 Δ*pdhR* ALE-2	This paper	A14F46I1R1
Escherichia coli K12 MG1655 Δ*pdhR* ALE-3	This paper	A15F51I1R1
Escherichia coli K12 MG1655 Δ*pdhR* ALE-4	This paper	A16F49I1R1
Escherichia coli K12 MG1655 Δ*pdhR*: SD. G-A	This paper	Δ*pdhR*: SD. G-A
Chemicals, peptides, and recombinant proteins		
Hydrogen peroxide	Fisher scientific	H325
Critical commercial assays		
Pyruvate dehydrogenase assay kit	Sigma-Aldrich	MAK183
Deposited data		
DNaseq	NCBI SRA	PRJNA704191
RNaseq	NCBI GEO	GEO: GSE167389
Oligonucleotides		
aceE Protospacer sense oligo: AGCGTCAACGTTATTAGATAGATA	IDT	Guide RNA Protospacer sequence
aceE Protospacer antisense oligo: AAACTATCTATCTAATAACGTTGA	IDT	Guide RNA Protospacer sequence
aceE Donor F: CCAGGTCTCAGTG CGATTTTTCTGGTAAAAATTATCCA GAAGATG	IDT	Oligos to amplify the donor construct
aceE Donor R: CCAGGTCTCAGAGC AGCGGATAGCTGAACGAATACG	IDT	Oligos to amplify the donor construct
Negative ARMS FP: ACTCAACGTTATTAGATAGATATGG	IDT	ARMS primers for colony verification
ARMS RP: GTTCGAGGTCTTTTTTCGAC	IDT	ARMS primers for colony verification
Recombinant DNA		
pRed_Cas9_recA_Δpoxb300	GENSCRIPT USA INC GenScript USA Inc	N/A
Software and algorithms		
iModulons' computation	https://github.com/SBRG/precise-db	N/A
UTR Designer	https://pubmed.ncbi.nlm.nih.gov/23164579/	N/A
EMOPEC	https://pubmed.ncbi.nlm.nih.gov/26752768/	N/A
Escher	https://journals.plos.org/ploscompbiol/article?id=10.1371/journal.pcbi.1004321	N/A
ME-model simulations	https://github.com/SBRG/cobrame	N/A

RESOURCE AVAILABILITY

Lead contact

Further information and requests for reagents may be directed to, and will be fulfilled by, the corresponding author Dr. Bernhard Palsson (palsson@ucsd.edu).

Material availability

All bacterial strains generated in this study are available from the Lead Contact with a completed Materials Transfer Agreement.

Data and code availability

DNaseq and RNaseq data generated during this study are available at NCBI Sequence Read Archive (SRA accession number PRJNA704191) and Gene Expression Omnibus (GEO accession number GSE167389) respectively.

EXPERIMENTAL MODEL AND SUBJECT DETAILS

Bacterial strains and growth conditions

Bacterial strains and primers used in this study are listed in the Key resources table. *E. coli* K-12 MG1655 (ATCC 700926) with *pyrE/rph* 82 bp deletion strain was used as the wild-type (WT) strain (Anand et al., 2019a). P1 phage transduction method was used to generate the knockout strains (Thomason et al., 2007) and strain from Keio collection was used as a donor for the gene knockout cassettes (Baba et al., 2006). The point mutation in the pre-evolved Δ*pdhR* strain was introduced using a genome editing method based on the CRISPR/Cas9 system (Zhao et al., 2016). We used ALE-2 (evolved Δ*pdhR* strain) to amplify the donor construct bearing the desired mutation. The oligos used for this purpose are listed in the Key resources table. Amplification-Refractory Mutation System (ARMS) was used for colony screening (Little, 2001) and the screened colonies were further verified by Sanger sequencing. BioTek Elx808 Absorbance Reader was used for the growth profiling with 200 μL culture volume per well using a minimum of three biological replicates. Media components were purchased from Sigma-Aldrich (St. Louis, MO).

METHOD DETAILS

Computing the causes of growth rate limitation

To estimate how increasing the expression of PDC affects growth rate, we performed simulations using the iJL1678b-ME model (Lloyd et al., 2018). We simulated the maximum growth rate of *E. coli* over a range of fixed PDC formation rates, ranging from approximately 0.1 to 20 times the optimal formation rate corresponding to maximum growth on glucose minimal medium.

By fixing the complex formation rate, the model is forced to transcribe the required RNA, translate required proteins, while also accounting for the required gene expression machinery (RNAP, ribosomes, tRNA, etc.) and metabolic costs (nucleotides, amino acids, etc.). In other words, the systems-level cost of PDC synthesis is computed.

PDC is a large complex involving a total of 60 protein monomers to form a single complex. We thus tested if the large size of PDC exacerbates its impact on the growth rate at high expression levels. Using iJL1678b-ME, we modified the PDH complex to consist only of 3 monomers: a single copy each of AceE, AceF, and Lpd. We then performed the same simulation as with the normal PDC. We used the same effective rate constant as the normal PDC.

Adaptive laboratory evolution (ALE) and DNA resequencing

ALE was performed using 4 independent replicates of Δ*pdhR* strain. Cultures were serially propagated on M9 minimal medium with 4 g/L glucose at 37°C and well-mixed for proper aeration using an automated system that passed the cultures to fresh flasks once they had reached an OD_{600} of 0.3 (Tecan Sunrise plate reader, equivalent to an OD_{600} of ~1 on a traditional spectrophotometer with a 1 cm path length). Cultures were always maintained in excess nutrient conditions assessed by non-tapering exponential growth. The evolution was performed for a sufficient time interval to allow the cells to reach their fitness plateau. The total length of experimental evolution corresponds to ~300 generations.

A clone from the endpoints of evolved strains was picked for DNA resequencing (Anand et al., 2019b). Strains were grown in M9 minimal medium supplemented with 4g/l glucose. Cells were then harvested while in exponential growth and genomic DNA was extracted using a KingFisher Flex Purification system previously validated for the high throughput platform (Marotz et al., 2017). Shotgun metagenomic sequencing libraries were prepared using a miniaturized version of the Kapa HyperPlus Illumina-compatible library prep kit (Kapa Biosystems). DNA extracts were normalized to 5 ng total input per sample using an Echo 550 acoustic liquid handling robot (Labcyte Inc), and 1/10 scale enzymatic fragmentation, end-repair, and adaptor-ligation reactions carried out using a Mosquito HTS liquid-handling robot (TTP Labtech Inc). Sequencing adapters were based on the iTru protocol (Glenn et al., 2019), in which short universal adaptor stubs are ligated first and then sample-specific barcoded sequences added in a subsequent PCR step. Amplified and barcoded libraries were then quantified using a PicoGreen assay and pooled in approximately equimolar ratios before being sequenced on an Illumina HiSeq 4000 instrument.

Computational prediction of aceE expression

The prediction of *aceE* expression corresponding to the mutated Shine-Dalgarno sequence was performed using two predictive models: UTR Designer (Seo et al., 2013) and EMOPEC (Bonde et al., 2016); following the suggested guidelines.

Transcriptomics and iModulon decomposition

The strains were grown in a condition the same as that used during ALE. Total RNA was sampled from two biological replicates. RNA isolation, rRNA removal, sequencing library preparation, library preparation, and data analysis was performed as previously described (Anand et al., 2020).

iModulon decomposition was performed by independent component analysis as described earlier (Anand et al., 2020; Sastry et al., 2019). Ref. WT, GMOS, Δ*pdhR*, Ref. WT ALEs, Δ*ubiC* ALEs, RpoB mutants, and *oxyR* mutants (EC ALEs) data were retrieved from our earlier publications (Anand et al., 2019a, 2020; Sastry et al., 2019).

Escher based quinone redox node activity analysis

The web-based tool for visualizations of metabolic pathways, Escher, was used for monitoring the transcriptional status of the respiratory quinone redox node using the average TPM counts.

Pyruvate dehydrogenase activity assay

E. coli strains were grown in M9 minimal medium with 4 g/L glucose at 37°C to an OD_{600} ~0.6. Cells from 5 mL culture were harvested by centrifugation (5-minute, 5000 rpm at 4°C), washed twice with 9 g/l NaCl and stored as cell pellets at −20°C overnight. Cell pellets were resuspended using 5 mL PDH assay buffer to obtain OD_{600} of 5 and were permeabilized with 50 μl chloroform and vortexed for 5 s. 5 μl of the permeabilized cells were used to perform the assay using the Pyruvate dehydrogenase assay kit (Sigma-Aldrich MAK183) as per manufacturer's protocol. The reaction mix was incubated at 37°C and then absorbance at 450 nm was measured using Tecan Infinite M200 Pro Plate Reader. The assay was performed with five replicates.

Phenotype characterization

Phenotype characterization was performed using three independent biological replicates. Culture density was measured at 600 nm absorbance with a spectrophotometer and correlated to cell biomass. Samples for the substrate uptake and secretion rate were filtered through a 0.22 μm filter (PVDF, Millipore) and measured using refractive index detection by HPLC (Agilent 12600 Infinity) with a Bio-Rad Aminex HPX87-H ion exclusion column. The HPLC method was the following: injection volume of 10 μL and 5 mM H_2SO_4 mobile phase set to a flow rate and temperature of 0.5 mL/min and 45°C, respectively.

Metabolic Flux Mapping

We used FoldME, a genome-scale model of metabolism and protein expression, to elucidate the metabolic shifts between the WT, Δ*pdhR*, and evolved strains. FoldME was used for ME-model simulations as it has shown to provide accurate depictions of proteome composition through the integration of the protein-folding network for *E. coli* (Chen et al., 2017).

The model was constrained with all phenotypic characterization data (i.e., growth rates and exchange rates), in addition to transcript mass fractions of major metabolic pathways calculated from RNA-seq data (Table S4). Imposing the mass fractions directly onto the model yielded infeasible solutions due to disparities between the mass fractions and phenotypic data. Considering that the mass fraction of ribosomal proteins scales linearly with growth rate (Scott et al., 2010, 2014), we generated the following constraints for integrating the transcriptomic profile:

$$\phi_r \cdot V_{pathway} \geq \phi_{pathway} \cdot V_r \quad (1)$$

$$V_{pathway} = \sum_i mw_i \cdot V_i^{translation} \quad (2)$$

$$V_r = \sum_i mw_{rProtein_i} \cdot V_{rProtein_i}^{translation} \quad (3)$$

Where ϕ_r and $\phi_{pathway}$ represent the transcript mass fraction of ribosomal protein and the major pathway of interest, respectively. Additionally, mw_i and $V_i^{translation}$ represent the molecular weight and translation flux of the *i*th protein in the corresponding pathway, whereas $mw_{rProtein_i}$ and $V_{rProtein_i}^{translation}$ represent the molecular weight and translation flux for the *i*th ribosomal protein.

QUANTIFICATION AND STATISTICAL ANALYSIS

Prism (GraphPad) version 9 was used for quantification and generation of plots. The mean with individual replicate values were plotted. The mean with standard deviation among three independent replicates is plotted for the peroxide sensitivity estimation.